POLITECNICO DI TORINO
Repository ISTITUZIONALE

VAT 3D printing of polymerizable ionic liquids for VOC capture

*Original*
VAT 3D printing of polymerizable ionic liquids for VOC capture / Armandi, M., Tosetto, B., Roppolo, I., Chiappone, A.. - In: NPJ ADVANCED MANUFACTURING. - ISSN 3004-8621. - 2:1(2025), pp. 1-12. [10.1038/s44334-025-00041-0]

*Availability:*
This version is available at: 11583/3017523 since: 2026-11-04T15:51:55Z

*Publisher:*
Springer Nature

*Published*
DOI:10.1038/s44334-025-00041-0

*Terms of use:*

This article is made available under terms and conditions as specified in the corresponding bibliographic description in the repository

*Publisher copyright*

(Article begins on next page)

21 November 2026

npj | advanced manufacturing

Article

https://doi.org/10.1038/s44334-025-00041-0

# VAT 3D printing of polymerizable ionic liquids for VOC capture

Check for updates

Marco Armandi[1,5], Beatrice Tosetto[1,2,3,5], Ignazio Roppolo[1,3] ✉ & Annalisa Chiappone[4]

Volatile Organic Compounds (VOCs) are threats to human health, therefore, developing systems that can trap them is of primary interest. The strategies exploited, such as powder beds, active carbons, or liquid systems, are effective but limited by the complexity of manipulating such systems. To tackle this problem, here, 3D printable systems based on photocurable polymerizable ionic liquids (PILs) are proposed. Several photocurable formulations were developed and the most promising were employed in Digital Light Processing (DLP) 3D printing, which allowed the fabrication of complex objects with high precision and fidelity (mean error value lower than ±0.12 mm). Finally, the ability of those 3D printed structures to trap VOCs such as acetone and acetonitrile was studied in detail by gravimetric testing (absorption capacity up to 21.6 wt% for Acetone and 17.4 wt% for Acetonitrile), and the nature of solvent-polymer interaction was investigated by FTIR spectroscopy, resulting to be completely reversible.

Volatile Organic Compounds (VOCs) are a large group of organic chemicals with high vapor pressures and boiling temperatures below 250 °C, meaning they easily evaporate, enriching the air with their presence in the gas form[1]. They encompass a broad range of organic chemicals, including hydrocarbons, alcohol, ketones, and also halogenated and aromatic compounds. Those molecules are emitted from a wide variety of sources, both natural and anthropogenic[2], ranging from industrial processes such as painting, chemical manufacturing, and petroleum refining to consumer products, e.g., paints, cleaning agents, adhesives, and personal care products[3]. The chemical nature of VOCs, together with their volatility, represents a serious threat to human health[2–5]. Additionally, VOCs play a significant role in the formation of ground-level ozone and smog, contributing to air quality degradation and environmental impacts[6]. Due to these detrimental effects, many countries have implemented regulations to limit VOCs emissions from industrial processes, consumer products, and vehicle exhaust[7,8]. At the same time, in the pursuit of sustainable solutions for environmental remediation, the development of advanced materials capable of efficient VOCs capture has emerged as a critical imperative[1,9].

Various methods are nowadays employed for the remediation of VOC-contaminated air and water[1], including capturing technologies onto porous materials[10–12], or liquid sorbents[13,14] and VOCs abatement through catalytic oxidation[15,16], biological degradation[17,18], and thermal or physical treatments[19,20]. The choice of remediation method depends on factors such as the type and concentration of VOCs, the volume of contaminated media, and the economic feasibility, and the best solution should be selected case by case[1,9].

Among the diverse materials investigated for VOCs adsorption, ionic liquids (ILs) have garnered considerable attention due to their tunable chemical structure and affinity for a wide range of organic compounds. In many cases imidazolium-based ionic liquids are used for this purpose, as they presented sufficient compatibility with the chemical structure of the organic solvents: for example [2-Mim][$NTf_2$] was combined with activated carbons and demonstrated excellent ability in ammonia adsorption of protic [MIM] [$NTf_2$], while aprotic [EMIM] [$NTf_2$] were studied for the capture of aromatic VOCs showing the importance of the CH- ·π and ·π ·π interactions for this kind of capture[21]. Moreover, imidazolium ionic liquids were also recently studied for the capture of low-carbon alcohol vapors from printing ink exhaust gases[22], and Imidazolium-based ILs supported membranes were proposed for VOCs separation, as well as for ethylene-ethane separation[23], propylene- propane[24,25] olefine- paraffine[26,27]. In practical applications, since ILs are not self-supporting, they are used either in liquid batches[28] or can be integrated into functional materials by impregnating polymeric membranes or by immobilization within hollow or porous polymeric fibers and films[29,30].

Polymerizable ionic liquids (PILs) can overcome this limitation because they have the great advantage of gathering the excellent properties of ionic liquids in terms of stability and chemical affinity to other molecules, together with the polymers' processability and ease of handling; therefore, PILs have increased their importance in recent years[29,31]. Furthermore, using different substituents on PILs or copolymers and crosslinkers allows a vast

[1]Dipartimento di Scienza Applicata e Tecnologia, Politecnico di Torino, Turin, Italy. [2]Department of Chemistry, Biology and Biotechnology, University of Perugia, Perugia, Italy. [3]Center for Sustainable Future Technologies, Italian Institute of Technology, Turin, Italy. [4]Dipartimento di Scienze Chimiche e Geologiche, Università di Cagliari, Monserrato, Italy. [5]These authors contributed equally: Marco Armandi, Beatrice Tosetto. ✉e-mail: ignazio.roppolo@polito.it

tuning of the materials' properties and architectures, impacting, for instance, on free volume and network glass transition temperature ($T_g$), which influence the interaction with gases and pollutants[32,33]. PILs in the form of membranes were also used for VOCs trapping[34], and organic gas separation[35,36].

Most of the polymers based on PILs are obtained via radical-induced polymerization of the vinyl or acrylic moieties present on the monomers; this means that those materials can also be synthesized via photoinduced reactions[37]. This additional versatility in processing opens up to the possibility of employing light-induced 3D printing techniques to shape PILs with complex geometry ad-hoc designed to suit the application[38–40].

These techniques are known as VAT 3D printing, and this general term refers to a group of 3D printing technologies based on the light-triggered and spatially controlled polymerization of liquid precursors contained in a reservoir. The fact that the starting material is a liquid monomeric mixture implies that the tailoring materials properties is particularly easy[41,42]. Among these techniques, the most common are Stereolithography (SLA), Masked Stereolithography (mSLA), and Digital Light Processing (DLP)[43]. From a technological point of view, the 3D object is obtained by subsequential light-irradiations, in which the light pattern projected corresponds to a sliced cross-section of the desired 3D design and induces a spatially controlled resin polymerization[44]. The fabrication of the 3D object usually occurs layer by layer, starting on a build platform that moves stepwise. Among the possible technologies, DLP was employed in this work since, compared to other 3D printing techniques, it offers unique advantages such as higher printing resolution and accuracy, the possibility to fabricate very complex structures without the need for supports or sacrificial materials, high rate of fabrication, and smoother surface finish[45].

In this context, DLP 3D printing is nowadays a well-established technology, especially for the fabrication of functional materials, as witnessed by the large literature in different application areas, including microfluidics[46], hydrogels[47], and bioapplications[48], sensors[49,50], and actuators[51], photonics[52], and 4D printing[53,54]. The convergence of innovative material design and 3D printing offers a promising avenue for creating tailored adsorbent materials with enhanced performance characteristics.

Polymerizable ionic liquids have been recently studied as suitable monomers for VAT 3D printing for various applications[39] such as $CO_2$ technologies[33,55], electronics[56], biomedical[57], and sensors[58]. But to the best of our knowledge, never for VOCs trapping, an application field that can benefit from the application of additive manufacturing. In fact, the fabrication of complex geometries can allow the production of objects with a high surface-to-volume ratio, helping flux absorption.

Therefore, in this study, digital light processing (DLP) 3D printing was employed to fabricate PIL-based adsorbents with tailored morphologies. The printed polymers have been characterized in terms of reactivity and thermomechanical properties; the printability of different formulations has been investigated. Subsequently, a systematic evaluation of polymers-VOCs interactions has been performed through an FT-IR study that was innovatively applied to the online evaluation of the vapor absorption properties, giving insights into the structure-property relationships governing polymers-VOCs interactions.

## Results

### 3D printing and materials characterizations

The different formulations described in Table 3 in Methods section were prepared aiming at evaluating the influence of PILs on the behavior and the VOCs absorption capacity of polymeric matrices. An imidazolium-based IL bearing a vinyl group was chosen as a monofunctional monomer, while two PEG-based bifunctional acrylates with different molecular weights and polarity were used as crosslinkers to obtain thermoset and 3D printable materials; the neat polymers' behavior was also studied as a comparison. Furthermore, the possibility of substituting the PEG-based acrylates using a bifunctional polymerizable ionic liquid bearing two vinyl groups as a crosslinker was also evaluated. For completeness, an additional formulation composed of M.IL (90 wt%) and PEGDA 250 (10 wt%) was prepared, but the cured material was too brittle to handle and not suitable for manipulation, therefore this was not considered in other experiments. Additionally, it must be noted that Bifunctional IL (B.IL) is in solid form, and the formulation $Bil_{10}Mil_{90}$ represents the composition with the highest amounts of B.IL soluble in M.IL without adding other solvents.

At first, the reactivity of the prepared formulations was evaluated by means of photorheology. This test allows the monitoring of the values of the storage modulus G' and the loss modulus G" in a function of time during the irradiation of the formulation and indicates the suitability of the formulations for DLP printing. Figure 1a shows the comparison among the G' plots obtained for the materials: in general, the considered formulations completed the photopolymerization process efficiently and in a relatively short time, within 15 s for 200 μm thick samples. The fast increase of the G' curve, which starts quite immediately after the irradiation with visible light, indicates that the formulations are suitable for the 3D Printing process since fast gelation times are preferred[33]. The presence of the ionic liquid monomer (M.IL) up to 50 wt% does not significantly influence the polymerization rate of PEGDA, both 250 and 575 (respectively formulation P2 and P5), as the slope of the linear part of each curve is similar, nor it delays the initiation of the reaction. On the other hand, the further increase of the amount of M.IL up to 90%, with the subsequent reduction of the crosslinker (PEGDA 575) down to 10 wt%, causes a slight decrease in the slope of the curve (formulation $P5_{10}Mil_{90}$), that in any case show an increase of 5 order of magnitude of G' in less than 10 s, and reaches its plateau in about 20 s. Therefore, also this formulation can also be considered suitable for vat 3D printing, even if longer irradiation times are expected.

In the case of the fully ILs-based formulation ($Bil_{10}Mil_{90}$), the polymerization appears delayed, and the reactivity is decreased, as evidenced by the lower slope of the curve compared to the other formulations. This can be attributed to the well-known lower reactivity of vinyl groups than the acrylic ones, which are instead present in PEGDA-based formulations[59]. Nevertheless, upon long exposure time (>60 s), a storage modulus of about $10^4$ Pa is reached, indicating the possibility to obtain self-standing printed materials after carefully evaluating the printing parameters.

Furthermore, when observing the trends of G' and G" for each sample (Fig. 1b reports the plot of sample $P5_{10}$-$Mil_{90}$ as an example; see Fig. S1 for the other curves), it is possible to see that at the end of the reaction, the storage modulus is higher, constant and greater than the loss modulus: this means that the material behaves more like a rigid solid, rather than being a viscous liquid. The graphs also represent the gel point of each formulation, which is the crossover point between G' and G".

Summarizing, the photorheology analysis performed showed that the tested formulations are all potentially suitable for VAT 3D printing; nevertheless, it must be noted that this test gives an indication of the behavior of the formulations in 3D printing, but actual processing parameters must be fixed in the 3D Printer.

Therefore, DLP printing parameters (layer thickness, light intensity, and exposure time) were empirically optimized to obtain 3D objects. The optimized values are reported in Table 3 in Methods section. Those were fixed by minimizing printing times while maintaining good CAD fidelity. Simple flat samples were prepared for further characterizations, and more complex ones were obtained, confirming once more that these formulations are suitable for this additive manufacturing technique. It is important to note that optimizing printing parameters allows for avoiding the presence of printing defects such as delamination or warping.

In particular, rectangular specimens (Fig. S2) and more complex porous gyroid structures were produced with all the formulations with different dimensions, i.e., a diameter ranging from 5.5 mm to 2.5 mm and features in the order of hundreds of microns (Fig. 1c–m). Gyroid geometries were selected for two reasons: on the one hand, the high complexity demonstrates the capabilities of 3D DLP technology; on the other hand, these geometries present a high surface-to-volume ratio (5 × 5 gyroid: 5.7 $mm^{-1}$, 2.5 × 2.5 gyroid: 38.6 $cm^{-1}$), and therefore can expose a high area for gas trapping. The printing parameters were tuned according to the formulations, and this process reflected their different reactivity, which was

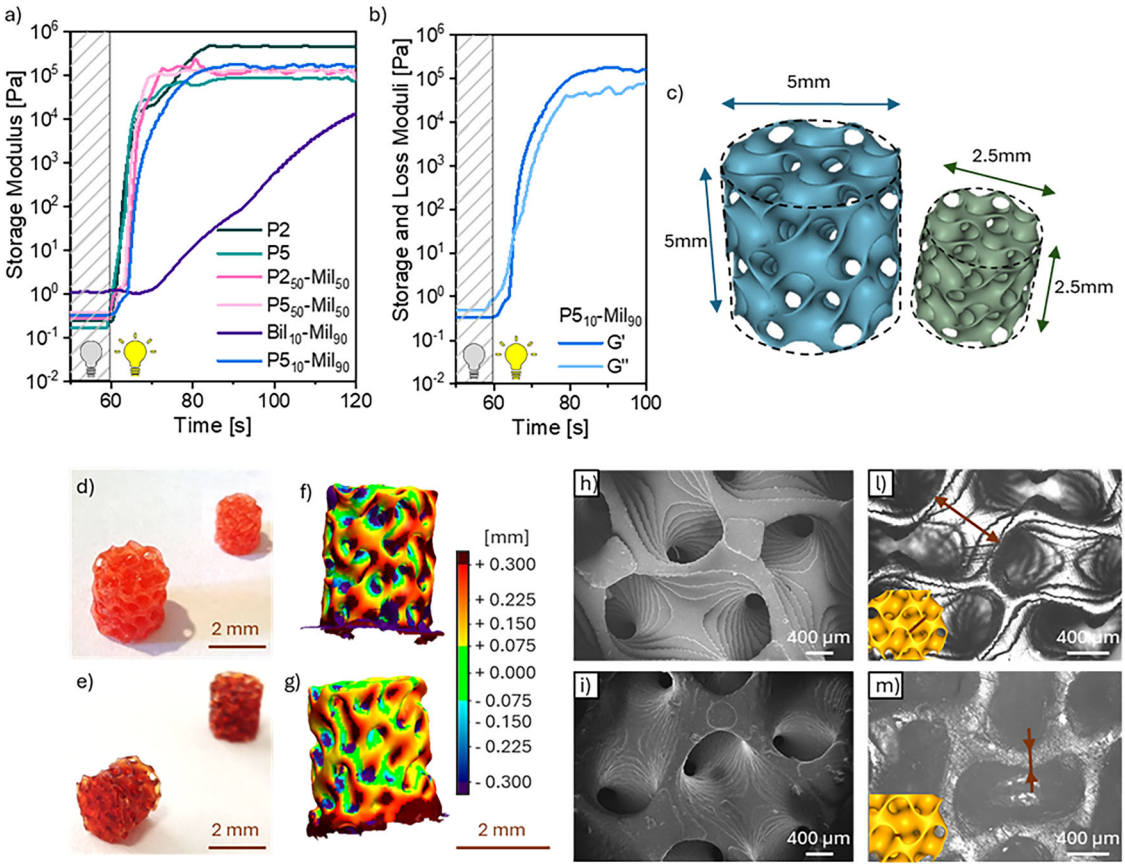



**Fig. 1 | 3D Printing characterization.** Photo-rheology results **a**: G'-all formulation, **b**: G', G"-P510-Mil90; **c**: Porous pellet CAD models; 3D printed samples **d**: P5, **e**: Bil10-Mil90; Printed samples and their fidelity color maps (**f**: P5, **g**: Bil10-Mil90). SEM images of the 3D printed porous pellets h: P5, **i**: Bil10-Mil90. Comparison of the porous pellets highlighted dimensions in the 3D printed sample (Optical Microscope pictures) and in the original CAD (**l**: P5 measured distance-red arrow- 690 µm, nominal value 700 µm, m: Bil10-Mil90 measured distance-red arrow- 166 µm, nominal value 150 µm).

already highlighted from photorheology analyses; in fact, while for all PEGDA-based formulations, the optimized printing parameters were similar for every object that has been realized, the formulations with a higher amount of ILs, needed different parameters for every shape. To improve the adhesion between the PILs and the building platform, an initial layer made of PEGDA was required during the fabrication of the pellets with formulations Bil$_{10}$-Mil$_{90}$ and P5$_{10}$-Mil$_{90}$. Every object has been built up with layers with a thickness of 50 µm, while the different light intensity and exposure times are reported in the Methods section (Table 3).

The quality of the printing process was evaluated by collecting images with FESEM and optical microscopy and checking the fidelity to the original CAD design by 3D scanning. Figure 1h and i report the SEM images of the gyroid structure built from formulations P2 (PEGDA 250) and Bil$_{10}$-Mil$_{90}$ (fully PILs), showing the porous interconnected structure in both samples. Sharp edges and no occlusion are present, supporting the statements of successful printing. Furthermore, it is evident that the formulations with PILs have smoother surfaces and a less pronounced layering effect, which can be connected to the kinetics of polymerization (vide infra). Figure 1l and m report the images collected with an optical microscope, and the distance between two significative points in the printed object has been compared with the one measured in the CAD model, resulting to be very similar both for the PEGDA and the PILs-based specimens.

Those tests reveal that PEGDA-based gyroid structures (formulation P5, Fig. 1h and l) have a slightly better definition than the one made of PILs (formulation Bil$_{10}$-Mil$_{90}$, Fig. 1i and m). This can be related to the higher reactivity of PEGDA, already measured with photorheology. In fact, higher reactivity is related to faster gelation points, which inhibits undesired propagation of polymerization out of the designed voxels. Nevertheless, PILs' objects (Bil$_{10}$-Mil$_{90}$) also present good resolution and high definition of complex shapes; although layers are less defined compared to P5 samples, they result in a smoother connection between each other. To strengthen these statements, the PEGDA and the PILs-based samples were analyzed by 3D scanning, and the obtained images were overlapped to the CAD design, giving fidelity color maps reported in Fig. 1f (P5) and 1 g (Bil$_{10}$-Mil$_{90}$). For both samples, CAD fidelity is good, with a mean error value of ±0.09 mm for the PEGDA sample (P5) and ±0.12 mm for the PILs one (Bil$_{10}$Mil$_{90}$). It must be noted that the real difference in the object could be lower since the calculation is influenced by the differences measured in the bottom parts of the samples, which are higher (>0.25 mm) due to the need for a longer exposure time to promote the attachment to the build platform. Those discrepancies obviously increase the average measured value.

The printed samples were then submitted to FT-IR ATR analysis and solvent extraction to evaluate the extent of photopolymerization in the 3D printing process, measuring both the conversion degree of C = C double bonds and the gel content (Table 1). The spectra on which the conversions were calculated are reported in the Supporting Information file (Fig. S3).

In good agreement with photorheology measurements, PEGDA monomers (samples P2 and P5) present high reactivity with high conversion of the acrylic double bonds and almost complete crosslinking, witnessed by the gel content >97% for both formulations. The high acrylic conversion is still maintained in the samples containing 50 wt% of monofunctional ionic liquid (P2$_{50}$-Mil$_{50}$ and P5$_{50}$-Mil$_{50}$), together with a high vinyl conversion. Furthermore, the samples obtained with those formulations exhibited very high vinyl conversion (>90%). On the other hand, in both cases, gel content is slightly lower than that of fully acrylic materials (P2 and P5). This can be consistent with a certain degree of homopolymerization of monofunctional monomers, which can then be extracted. The same behavior can be noticed in the sample based on the formulation P5$_{10}$-Mil$_{90}$,

**Table 1 | Conversion values, gel content, glass transition temperature ($T_g$), and E' at 25 °C of the tested formulations**

| Sample | Double bond conversion (%) | | Gel Content (%) | $T_g$ (° C) | E'@25 °C (MPa) |
|---|---|---|---|---|---|
| | Acrylic@1665 $cm^{-1}$ | Vinyl@995 $cm^{-1}$ | | | |
| P2 | 87 | -- | 99 | 67 | 1025 |
| P5 | 99 | -- | 97 | −20 | 30 |
| $P2_{50}$-$Mil_{50}$ | 87 | 99 | 88 | 45 | 198 |
| $P5_{50}$-$Mil_{50}$ | 90 | 90 | 85 | −7 | 14 |
| $Bil_{10}$-$Mil_{90}$ | – | 76 | 95 | 47 | 80 |
| $P5_{10}$-$Mil_{90}$ | 87 | 95 | 89 | 24 | 22 |

composed of 90% monofunctional ILs. Last, it must be noted that in the formulation $Bil_{10}$-$Mil_{90}$, the conversion of vinyl groups was measured since it doesn't contain acrylic moieties. In this case, their conversion was lower than the value obtained for sample $P5_{10}$-$Mil_{90}$ in which there is also the presence of acrylates (respectively 76% vs 95%). This lower vinyl conversion despite the longer irradiation times (see Supporting Information file), can be explained considering the lower reactivity of vinyl groups compared to acrylic ones, which are less prone to be attacked by the photoinitiator[59]. On the contrary, it can be supposed that in the presence of acrylic moieties, which are very reactive towards photoinitiators, the vinyl moieties can also be attacked by growing macromolecules. This aspect can be of great interest for material design and would be a fundamental aspect that could be deepened in future research. Nevertheless, the gel content was very high, which can be explained considering that in this case polymerization was occurring only among vinyl moieties, and therefore, few crosslinking points may create insoluble networks.

DMTA was then employed to evaluate the thermomechanical properties of the 3D printed materials. The Elastic and loss moduli were measured, and together with tanδ plots, they are reported in Fig. S4, while the values of the glass transition temperatures ($T_g$) and the elastic modulus at 25 °C are reported in Table 1.

Analyzing the data obtained, it is possible to observe that addition of the monofunctional polymerizable ionic liquid to PEGDA 575 induces an increase of $T_g$ (P5: $T_g$ = −20 °C | $P5_{50}$-$Mil_{50}$: $T_g$ = −7°C|$P5_{10}$-$Mil_{90}$: 24 °C), a broadening of tanδ, while mechanical properties at room temperature are quite similar (30 MPa, 14 MPa and 22 MPa respectively). This can be related to a twofold effect: the presence of ionic interactions between PILs may induce a stiffening in the very soft PEGDA 575 matrix, which is mitigated by the decrease of crosslinking density caused by the addition of monofunctional monomers. Differently, when the M.IL is added to a matrix that has $T_g$ higher than room temperature as PEGDA 250 (formulations P2 vs $P2_{50}$-$Mil_{50}$), the decrease of the crosslinking density seems to play a major role leading to the decrease of the $T_g$ (67 °C vs 45 °C), keeping the broadening of tanδ, and the reduction of the E' at 25 °C.

The material completely based on PILs ($Bil_{10}$-$Mil_{90}$) is characterized by a broad $T_g$ range that starts at about 20 °C and presents its maximum above 40 °C, indicating that the material at room temperature is close to its $T_g$. Unfortunately, at temperatures above 60 °C, the material presents a complete loss of mechanical properties, which can be visualized by the fast decrease of E'. This decrease leads to a fast increase of tanδ, bringing to an unusual curve for a thermoset. This loss of mechanical properties represents an evident criticism for using these materials at high temperatures, and it could be explained by considering a temperature-induced decrease of ionic interactions among the chains, which results in a loss of consistency. This speculation should be demonstrated with dedicated experiments, which are out of the scope of the study, but those are relevant challenges for developing these materials for applications at high temperatures. Having fully assessed the fundamental properties of the synthesized materials, our interest moved toward defining the VOCs absorption properties.

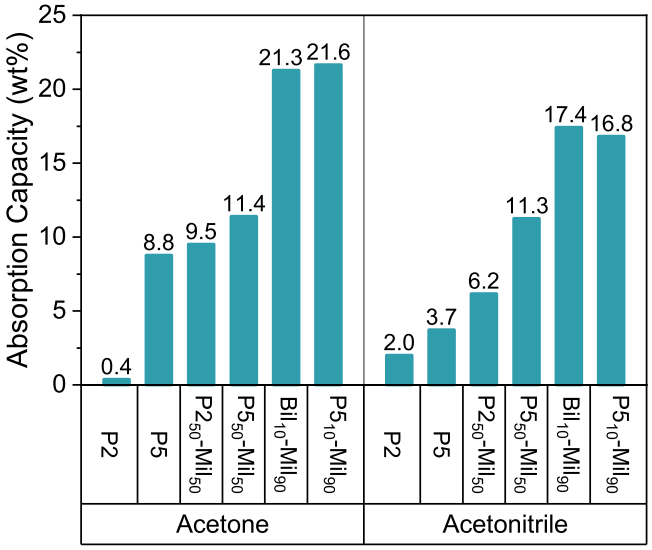



**Fig. 2 |** Gravimetric adsorption capacity measured at an equilibrium pressure of 175 mbar Ac and 90 mbar Acn and room temperature.

## Trapping properties

The gas permeation into a polymer matrix involves both the gas's solubility within the polymer and its diffusion throughout the material's volume. Consequently, the VOCs sorption capacity of 3D-printed PILs is influenced by various factors, including their chemical interactions and physical properties. The final PILs-VOCs interaction can't be easily predicted, and for this reason, some preliminary analyses were conducted to assess the affinity of the studied materials for the absorption of different VOCs (see Fig. S5). Among them, the employed PILs resulted in a higher absorption capacity of Acetone and Acetonitrile, so those VOCs were selected for more comprehensive quantitative and qualitative studies. Quantitative VOC adsorption tests performed on 3D printed gyroid pellets were repeated with Acetone (Ac) and Acetonitrile (Acn) at constant and controlled pressure and room temperature; the results are reported in Fig. 2, while a comparison with the preliminary data is reported in Fig. S6. Since the preliminary tests were conducted at 40 °C to increase the vapor pressure of the tested organic pollutants, this comparison effectively highlights the temperature effect. This effect is related both to the different VOCs concentrations, which lead to a significant increase in absorption for all VOC/polymer combinations, and to variations in the physical state of the polymers. For instance, materials $P2_{50}$-$Mil_{50}$, $Bil_{10}$-$Mil_{90}$, and $P5_{50}$-$Mil_{50}$ have a glass transition temperature close to that used for this preliminary testing. It must be noted that the selected temperature (40 °C) well-fits the temperature constraints previously defined by DMTA.

Figure 2 shows the amounts of Ac and Acn adsorbed at 298 K onto polymer films upon exposure to an equilibrium pressure of 174 mbar Ac and 90 mbar Acn. The samples adsorbing the highest amounts of both solvents were those prepared with M.IL 90 wt.%, *i.e.* $P5_{10}$-$Mil_{90}$ and $Bil_{10}$-$Mil_{90}$, with adsorption capacities of 21.3 wt.% (3.67 mmol $g^{-1}$) and 21.6 wt.% (3.72 mmol $g^{-1}$) for Ac, and 17.4 wt.% (4.24 mmol $g^{-1}$) and 16.8 wt.% (4.09 mmol $g^{-1}$) for Acn, respectively. In contrast, the sample prepared with PEGDA 250 (P2) alone showed negligible amounts of adsorbed Ac and Acn. In general, samples prepared with P5 (alone or in combination with M.IL) showed higher trapping capacities than the corresponding ones prepared with P2. This can be related to the higher mobility in P5-based formulations, witnessed by the lower $T_g$ compared to P2-based ones. This higher mobility may provide a rearrangement capability of the polymeric network, consequently leading to the entrapment of greater amounts of VOCs, as already observed in previous publications[60,61].

Although some conventional adsorbents such as activated carbons, zeolites, and MOFs exhibit higher adsorption capacities[62], these values were

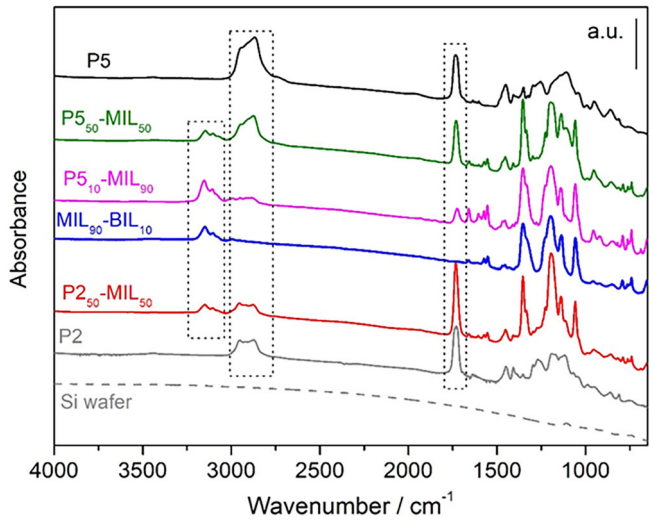



**Fig. 3 | FTIR spectra of polymer films outgassed under vacuum at RT for 1 h.** The highlighted vibration bands are: 1738 cm$^{-1}$ (stretching $\nu_{CO}$), 3000–2870 cm$^{-1}$ (stretching $\nu_{CH2}$), 3085–3150 cm$^{-1}$ (imidazolium ring).

typically obtained after thermal pre-treatment at 150–300 °C to remove pre-adsorbed atmospheric species. For instance, a zeolite Y degassed at 300 °C adsorbed approximately 6 mmol g$^{-1}$ of acetone at 20 °C under comparable pressure conditions[63], a graphene oxide/MIL-101 composite activated at 150 °C reached about 17 mmol g$^{-1}$ [64], and high adsorption capacities up to 18.7 mmol g$^{-1}$ were reported for activated carbons outgassed at 300 °C[65]. In contrast, the samples investigated in this study were only degassed at room temperature, yet still achieved significant adsorption capacities for both Ac and Acn. This highlights the practical advantage of these materials in terms of lower energy requirements and operational simplicity, which may be particularly relevant for real-world applications where mild regeneration conditions are preferred.

### FTIR spectroscopic investigation of Ac and Acn adsorption

To investigate the nature of the adsorbate-adsorbent interaction, the optical adsorption isotherms of the two solvents were measured by means of transmission FTIR spectroscopy. To this end, proper B-doped Si wafers transparent to IR radiation were coated with thin polymer films with different formulations. Blank gravimetric experiments with bare Si wafers confirmed the absence of solvent adsorption contributions from the wafers themselves. Specifically, the difference in weight between a cell containing both the Si wafer and solvent vapor, and a cell containing only solvent vapor at the same equilibrium pressure matched the mass of the wafer. Therefore, any changes in IR spectra observed in the blank FTIR experiments (i.e., spectra of Si wafer exposed to increasing pressures of solvent vapors, as described in the next sections) were exclusively due to the solvent vapor in the cell.

The spectra of the bare polymer films outgassed and kept under vacuum (recorded before exposure to Ac or Acn vapors) are reported in Fig. 3. The PEGDA-based formulations (P2 and P5) show typical strong absorption bands due to ester (stretching $\nu_{CO}$ at 1738 cm$^{-1}$) and -CH$_2$- groups (stretching $\nu_{CH2}$ at 3000–2870 cm$^{-1}$, and bending $\delta_{CH2}$ at 1470 cm$^{-1}$).

The samples prepared by adding M.IL (or B.IL) in the formulation show additional bands at 3152, 3106, and 3085 (shoulder) cm$^{-1}$ related to the imidazolium ring. The assignment of these bands is not straightforward since Fermi resonance of C–H stretching modes with combinations and overtones of ring vibrations causes complicated vibrational signatures in this spectral region[66]. All figures presented in the following sections show different spectra, i.e., obtained by subtracting the spectrum of the bare samples under vacuum (i.e., before solvent dosage) from all the spectra taken under increasing solvent equilibrium pressure.

### Adsorption of Acetone

The adsorption of Ac was followed by monitoring changes in the spectral region of the $\nu_{CO}$ mode of Ac. Gaseous Ac presents a strong and complex roto-vibrational profile centered at 1738 cm$^{-1}$ ($\nu_{CO}$ mode), along with two bands at 1436 and 1366 cm$^{-1}$ ($\delta_{CH3}$ modes). These bands were clearly observed in the blank experiment with the bare Si wafer (Fig. S7), i.e., when no adsorption occurs.

As expected from gravimetric measurements, a negligible Ac adsorbed amount was observed with the P2 sample, which basically showed identical spectral features of the bare Si wafer (Fig. S8). In contrast, additional $\nu_{CO}$ bands due to adsorbed Ac were detected in all other samples. Figure 4 shows the difference spectra in the $\nu_{CO}$ region relative to Ac adsorption onto selected samples under equilibrium pressures between 4.5 mbar ($p/p^\circ \approx 0.012$) and 175 mbar ($p/p^\circ \approx 0.47$). In the P5 sample (Fig. 4a), the sharp $\nu_{CO}$ band related to the adsorbed Ac and positioned at 1710 cm$^{-1}$ overlaps with that of the gas. The band's position does not vary with coverage. The strength of Ac interaction with an adsorbent surface is generally evaluated by the frequency downward shift $\Delta\nu_{CO}$ with respect to the liquid (i.e., 1717 cm$^{-1}$) rather than the gas because the transition to a condensed phase yields an intrinsic downward shift of the $\nu_{CO}$ mode. The observed $\nu_{CO}$ frequency suggests a weak interaction of the adsorbed Ac molecules with the surface ($\Delta\nu_{CO} = 7$ cm$^{-1}$). Similar frequencies were observed for Ac H-bonded to isolated hydroxyls of silica[67,68] or coordinated to weak $Na^+$ Lewis sites in zeolites[69]. Also diluted acetone solutions (~3.5 vol %) in polar $CHCl_3$ present a main band centered at ~1710 cm$^{-1}$[70]. In the present case, it is likely that the surface polar groups of P5 (i.e., oxygen atoms of ether and/or ester groups) weakly interact with the dipole moment of Ac. The weak nature of the interaction was also suggested by the type of optical isotherms obtained (see below), as well as by the complete reversibility of adsorption at RT. Indeed, a short evacuation at RT caused the complete disappearance of the spectral features of adsorbed Ac (dotted curves in Fig. 4a–e) When M.IL is added to the P5-based formulation (P5$_{50}$-Mil$_{50}$ and P5$_{10}$- Mil$_{90}$ in Fig. 4c, d, respectively), the $\nu_{CO}$ band of adsorbed Ac appears definitely broader and seems to include some components at low wavenumbers (up to ca. 1700 cm$^{-1}$). On the P5$_{10}$-Mil$_{90}$ sample, the band intensifies rapidly, surpassing the gas-phase band even at low coverage. The maximum at low coverage is still found at 1710 cm$^{-1}$, but shifts towards higher frequencies at high coverage. The frequency observed at the highest equilibrium pressure (1715 cm$^{-1}$) is characterized by an almost zero $\Delta\nu_{CO}$, and can be ascribed to the gradual build-up of a liquid-like Ac phase formed upon adsorbate-adsorbate interactions[68]. This feature is common to almost all M.IL-based formulation, being definitely more evident for Bil$_{10}$- Mil$_{90}$ sample (Fig. 4d, with maximum at 1719 cm$^{-1}$). The cross-linked polymeric network obtained in the presence of M.IL (and even more of B.IL) may favor the multi-layer adsorption of Ac. Finally, it is worth noting that the beneficial effect of IL was also observed when PEGDA250 was used as a cross-linker. In fact, while Ac was not adsorbed on the P2 sample, the P2$_{50}$-Mil$_{50}$ sample exhibited a gravimetric adsorption capacity comparable to that of its counterpart, P5$_{50}$Mil$_{50}$. However, the spectral features displayed by P2$_{50}$-Mil$_{50}$ (i.e., a sharp band at 1710 cm$^{-1}$, as shown in Fig. 4b) resemble those of P5 rather than those of the P5$_{50}$-Mil$_{50}$ sample.

In order to have a semi-quantitative comparison of the adsorbed species on the different formulations, the spectra reported in Fig. 4a–d were computer-processed, subtracting the gas contribution and normalizing absorbances with respect to the actual film thickness (as described in the experimental section). As an example, the processed spectra corresponding to an equilibrium pressure of about 30 mbar are reported in Fig. 4e, showing significantly higher integrated absorbances for P5$_{10}$-Mil$_{90}$ and Bil$_{10}$-Mil$_{90}$ samples. Interestingly, no relevant differences among the different formulations are seen in the position of the maxima (1710 cm$^{-1}$), at least at medium-low coverage. This implies that most of the adsorbed species have similar interaction strengths, regardless of the formulation composition. Nevertheless, the band of M.IL-based samples exhibits a tail at low frequencies, indicating the presence of some adspecies characterized by stronger interactions with the polymer functionalities. The latter may

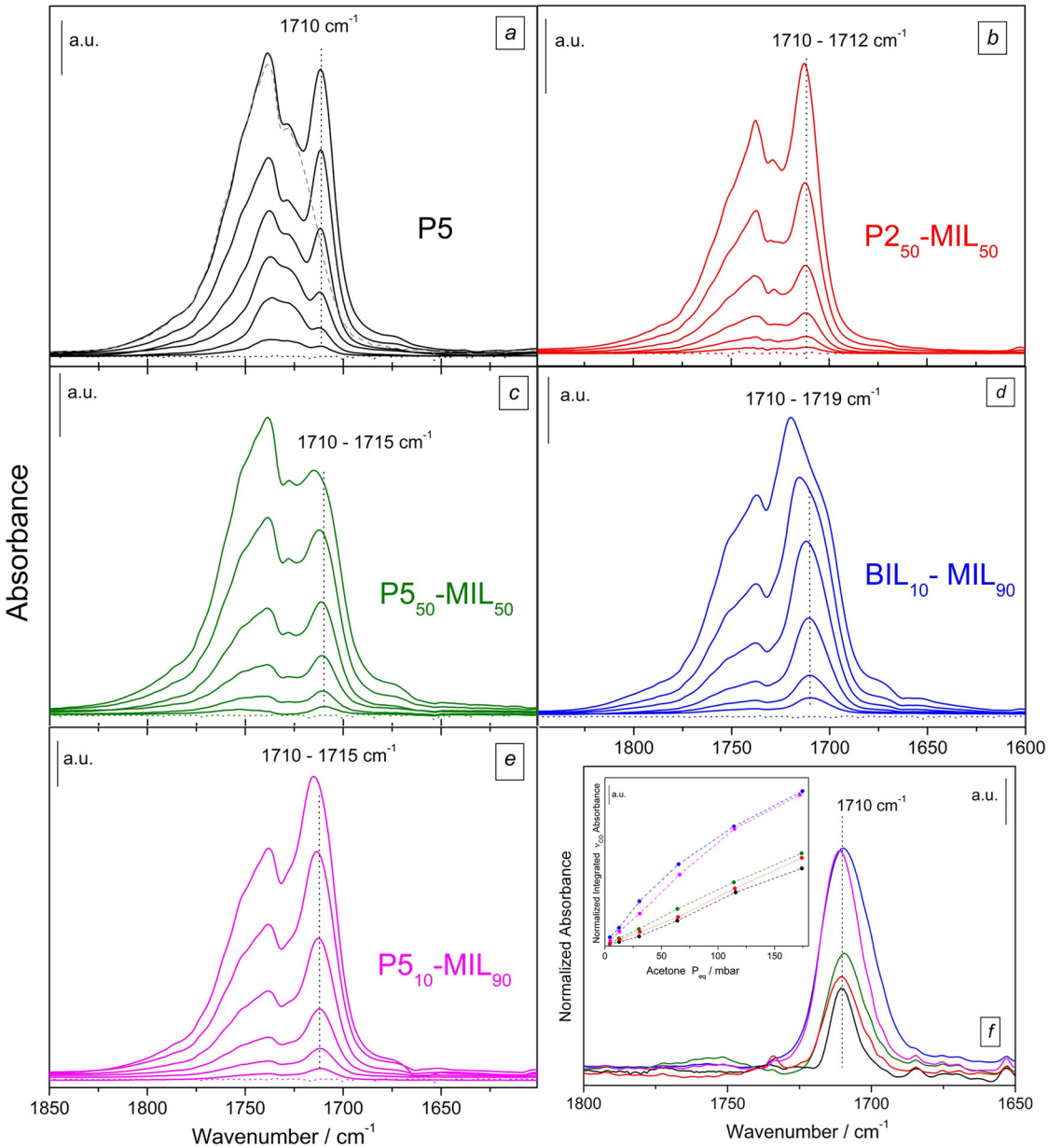



**Fig. 4 | Absorbance of Acetone.** Difference FTIR spectra at increasing Ac equilibrium pressure (Peq = 4 – 175 mbar) on **a** P5, **b** P250-MIL50, **c** P550-MIL50, **d** BIL10-MIL90, **e** P510-MIL90 sample. **f** Comparison of normalized difference FTIR spectra (after subtraction of gas contribute) taken at ca. 30 mbar Ac equilibrium pressure. The inset shows the optical isotherm obtained from normalized integrated absorbance of νCO at different equilibrium pressures.

include the positively charged imidazolium ring, as well as its counter anion. This feature is definitely more evident for the $Bil_{10}$- $Mil_{90}$ sample, suggesting that the use of B.IL instead of PEGDA as a cross-linker leads to a polymeric network in which the functionalities acting as stronger sites are more accessible to Ac.

The normalized integrated absorbances measured at different equilibrium pressures were used to plot the optical adsorption isotherms reported in the inset of Fig. 4e. The integrated absorbances measured at maximum equilibrium pressure are fairly consistent with the gravimetric adsorption capacities reported in Fig. 2. Minor discrepancies between the two measurements could be attributed to limitations in spectral processing and/or normalization of the integrated absorbances. The formulations containing M.IL ≤ 50 wt.% exhibit a linear adsorption isotherm of the Henry type, which is characteristic of weak adsorbate-adsorbent interactions. Based on the spectral features of the $\nu_{CO}$ band described above, the different slopes observed for the three samples could be mainly due to variations in the available surface rather than in the interaction strength. The occurrence of linear isotherms is, in principle, consistent with a process of absorption (e.g., a solubilization process) rather than adsorption. After all, the surface of a polymer is a dynamic object undergoing rearrangements upon changes in the surrounding phase. The chemical affinity of the solvents likely plays a role in inducing conformational change at the polymer surface[71]. Therefore, the solvent ability to diffuse within the polymer network could be the main factor affecting the overall adsorption (or absorption) behavior. On the other hand, only the $Bil_{10}$- $Mil_{90}$ sample clearly shows a concave-downward isotherm, likely due to the occurrence of stronger specific interactions.

### Adsorption of Acetonitrile

The adsorption of Acn was followed by monitoring changes in the $\nu_{CN}$ stretching spectral region between 2320 and 2200 $cm^{-1}$. In this region, Acn vapor exhibits two unresolved roto-vibrational profiles resulting from Fermi resonance (FR) between the fundamental $\nu_{CN}$ stretching (Q band at

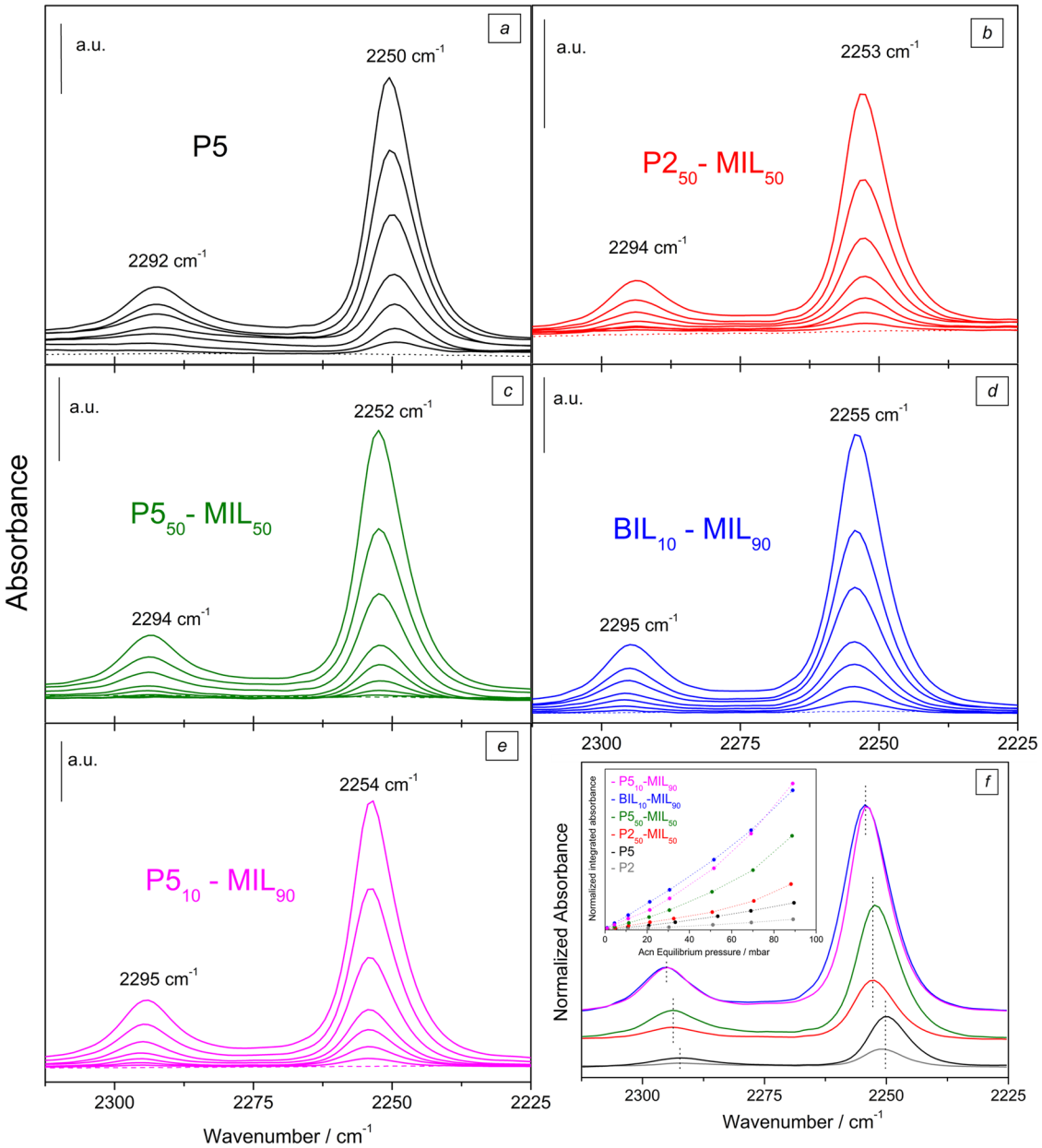



**Fig. 5 | Absorbance of Acetonitrile.** Difference FTIR spectra at increasing Acn equilibrium pressure on **a** P5, **b** P250-MIL50, **c** P550-MIL50, **d** BIL10-MIL90, **e** P510-MIL90 sample. **f** Comparison of normalized difference FTIR spectra recorded at ca 50 mbar Acn equilibrium pressure. For clarity, spectra are vertically shifted. The inset shows the optical isotherm obtained from normalized integrated absorbance of νCN at different equilibrium pressures.

2266 $cm^{-1}$) and the $\delta_{CH3} + \nu_{C-C}$ combination (Q band at 2306 $cm^{-1}$)[72]. Similar to the Ac measurements, the spectra from the Acn blank experiment (i.e., Acn dosage onto the bare Si wafer) showed only the contribution of the vapor phase. However, unlike in the Ac measurements, the signal intensity due to Acn vapor was significantly lower. Even for the sample adsorbing lower amounts of Acn (P2), the integrated absorbance due to the vapor was about 1% of that due to the adsorbed phase (Fig. S9). Therefore, subtracting the gas contribution from the spectra of Acn adsorbed onto polymer films was unnecessary. Figure 5 shows the difference spectra of Acn adsorbed onto selected samples under equilibrium pressures between 4.5 mbar ($p/p° \approx 0.03$) and 90 mbar ($p/p° \approx 0.57$). All samples show the characteristic doublet in a narrow frequency range, i.e., 2250–2255 $cm^{-1}$ for the low frequency component and 2292–2295 $cm^{-1}$ for the high frequency component, without any significant band shift with coverage. The band position of adsorbed Acn is generally compared to that of Acn in $CCl_4$ liquid solution, where the FR generates a doublet at 2296 and 2254 and $cm^{-1}$, with the latter band being more intense[73–75]. The position of the doublet has been shown to shift upwards with increasing electron withdrawal from the N lone pair upon adsorption. For example, weak interactions between Acn and hydroxyl groups of clay minerals give rise to reversible (at RT) bands at 2255 and 2297 $cm^{-1}$, whereas stronger interactions with acidic -OH in protonic zeolites result in a doublet at 2276 and 2305 $cm^{-1}$[75]. In the present study, the position of the doublet suggests a weak adsorbate-adsorbent interaction for all samples, as confirmed by the complete reversibility of the adsorption. Indeed, a short evacuation at RT caused the complete disappearance of the spectral features of adsorbed Acn (dotted curves in Fig. 5a–e). Adding M.IL to the formulations leads to a slight shift towards higher frequencies of both peaks, thus indicating the presence of adspecies characterized by a slightly stronger perturbation.

The different position of the doublet for different M.IL contents is clearly shown in Fig. 5f, which compares the normalized spectra recorded at an equilibrium pressure of about 50 mbar. This comparison also allows for

semi-quantitative analysis of the adsorbed species and agrees with the adsorption capacities observed in the gravimetric measurements. As with the spectra of adsorbed Ac, the measure of normalized integrated absorbances at different equilibrium pressures allowed obtaining the optical adsorption isotherms of Acn (inset of Fig. 5f). The five PEGDA-containing formulations exhibit type III isotherm, according to IUPAC classification[76]. These concave-upward isotherms are typically observed when adsorbed molecules cluster around the most favorable adsorption sites without forming a monolayer, indicating weak adsorbent-adsorbate interactions. Similar to Ac isotherms, the $Bil_{10}$-$Mil_{90}$ sample exhibits a slightly different behavior, showing an almost linear dependence of the adsorbed amount on the equilibrium pressure. This result, combined with the observed spectral features, agrees with the presence of stronger interactions for this sample. Overall, the comparison between Acn and Ac isotherm shapes indicates a lower affinity of most of the samples for Acn. This finding is not straightforward to interpret, especially given the larger Acn dipole moment ($\mu$ = 3.919 and 2.88 D for Acn and Ac, respectively[77]), a property that should, in principle, result in stronger dipole-dipole interactions with the polar surface of the polymers. A possible explanation is that the adsorbent-adsorbate interactions are significantly influenced by dispersive forces, which are stronger for Ac due to its higher polarizability (polarizability volume $\alpha$ = 4.28 and 6.27 Å$^3$ for Acn and Ac, respectively[77]).

In summary, the FTIR study of adsorbed Ac and Acn showed that most of the adspecies exhibit similar interaction strength. Only the samples containing 90 wt.% of M.IL showed the presence of stronger interactions, which were even more pronounced when B.IL was used as a cross-linker. The semi-quantitative analysis of the optical isotherms agrees with the adsorption capacities measured gravimetrically and suggests a higher affinity for Ac compared to Acn in most of the samples. This could be explained by assuming that the adsorbent-adsorbate interactions are significantly influenced by dispersive forces, which are stronger for Ac due to its higher polarizability.

## Discussion

In this study, different photocurable formulations based on photocurable PILs were studied, aiming at fabricating 3D printable materials with the ability to trap volatile organic compounds (VOCs).

In particular, a vinyl-imidazole based ILs (3-Ethyl-1-vinylimidazolium bis (trifluoromethanesulfonyl) imide, M.IL) was co-polymerized with 3 different crosslinkers, namely PEGDA 250, PEGDA 575, and a bifunctional ionic liquid (Butandyl-3,3'-[bis-(1-vinyl)-imidazolium] di-bis(trifluoromethanesulphonyl)imide, B.IL). Preliminary investigations showed that PEGDA 575 and B.IL allowed the successful fabrication of photocurable materials up to a ratio of 90 wt.% M.IL - 10 wt.% crosslinker (formulation $P5_{10}$-$Mil_{90}$), while for PEGDA 250, the maximum ratio was 50 wt.% - 50 wt.% (formulation $P2_{50}$-$Mil_{50}$). Photorheology measurements evidenced that the formulations based on acrylic crosslinkers are very reactive, enabling fast photopolymerization reaction even with a high content of M.IL. On the contrary, the formulation $Bil_{10}$-$Mil_{90}$, which was totally based on ionic liquids, presented delayed gelation and lower photoreactivity. Nevertheless, all the developed formulations were considered suitable for vat 3D printing and therefore were tested in Digital Light Processing (DLP) equipment.

3D printing parameters were optimized for all the considered formulations, and complex gyroid-like structures were fabricated, resulting in high precision (around 150 µm) and great CAD fidelity (around ± 100 µm). Furthermore, all the structures were easy to manage and did not show a tendency to crack or be damaged easily, since mechanical properties were suitable for the envisaged applications.

Finally, VOCs sorption capacities were investigated through gravimetric analysis, which revealed a particular affinity towards acetone (Ac) and acetonitrile (Acn). The nature of solvent-polymer interactions was examined using FT-IR spectroscopy of the adsorbed Ac and Acn. Samples formulated with PEGDA 575 (either alone or combined with M.IL) showed greater adsorption capacities compared to those prepared with PEGDA 250, likely due to the enhanced rearrangement capability of the former. The best absorption capacity was 21.6 wt% for Acetone and 17.4 wt% for Acetonitrile. All samples exhibited weak physisorption of both solvents, which was completely reversible at room temperature. Spectroscopic studies demonstrated that most of the species formed displayed similar interaction strengths, regardless of the formulation composition, and the overall adsorption capacity appears to be linked to the rearrangement capabilities of the materials. However, some adspecies with stronger interactions with the polymer functionalities were observed, particularly in $Bil_{10}$-$Mil_{90}$ samples, suggesting that the use of B.IL as a crosslinker creates a polymeric network where adsorption sites are more accessible.

Compared to other systems commonly used for VOCs trapping, such as active carbons of filtrating powders, the materials described here may show lower adsorption capacity, but, on the other hand, the system here developed has the advantages of ease of manipulation and ease of shaping, including very complex geometries as the gyroid structures here reported. Noteworthy, the absorption is completely reversible at room temperature by applying a mild vacuum, making those materials appealing in terms of reusability and competitive with more established methods, such as the ones mentioned above, which require the application of energy (usually thermal) for regeneration. By harnessing the synergistic advantages of DLP 3D printing and polymerizable ionic liquids, this work underscores the potential of additive manufacturing techniques for the creation of bespoke materials tailored to specific environmental remediation needs. On the other hand, these findings are just the first steps for the real applications of those materials: selectivity and competitive adsorption with other gases should be investigated, along with testing in harsher conditions such as elevated temperature. Next investigations will be focused on moving these exploratory findings on the ground, aiming at defining the precise conditions in which PILs-based 3D printed structures can be competitive with the more established technologies.

## Methods

### Materials

Poly(ethyleneglycol)diacrylate (PEGDA) Mw 250 and 575, phenylbis(2,4,6-trimethylbenzoyl) phosphine oxide (BAPO), and Methyl Red (MR) were purchased from Merck.

3-Ethyl-1-vinylimidazolium bis(trifluoromethanesulfonyl) imide (monofunctional IL/M.IL) and 1,4-Butandyl-3,3'-[bis-(1-vinyl)-imidazolium]di-bis(trifluoromethanesulphonyl)imide (bifunctional IL/B.IL) were purchased from Solvionic. Acetone, Isopropyl alcohol, Ortho-Dichlorobenzene, Acetonitrile, and Chloroform were purchased from Merck.

### Preparation of the formulations

Different formulations have been prepared containing different amounts of monofunctional IL and different crosslinkers. The compositions of the different formulations are summarized in Table 2.

BAPO and MR were added to all the formulations with a fixed concentration of 2 and 0.1 phr respectively (phr = per hundred resin).

### DLP 3D printing

Different objects were produced using a DLP-3D Printer (ASIGA Max UV 27) equipped with an LED light source @385 nm; maximum light

**Table 2 | Compositions of the investigated formulations**

| Sample | PEGDA250 (wt%) | PEGDA575 (wt%) | B.IL (wt%) | M. IL (wt%) |
|---|---|---|---|---|
| P2 | 100 | – | – | – |
| P5 | -- | 100 | – | – |
| $P2_{50}$-$Mil_{50}$ | 50 | – | – | 50 |
| $P5_{50}$-$Mil_{50}$ | – | 50 | | 50 |
| $Bil_{10}$-$Mil_{90}$ | – | – | 10 | 90 |
| $P5_{10}$-$Mil_{90}$ | – | 10 | – | 90 |

**Table 3 | 3D Printing parameters**

| Material | Layer Thickness | Light intensity ($mWcm^{-2}$) | Exposure time - first two layers (s) | Exposure time - other layer (s) |
|---|---|---|---|---|
| P2, P5, $P2_{50}$-$Mil_{50}$, $P5_{50}$-$Mil_{50}$ | 50 µm | 32 | 0.8 | |
| $P5_{10}$-$Mil_{90}$, $Bil_{10}$-$Mil_{90}$ | | | 2–3[a] | 1.5 |

[a]for gyroids 3 s of irradiation were needed to ensure adhesion with the platform due to the low layer's filling ratio.

intensity 50 $mW{\cdot}cm^{-2}$, pixel resolution 27 × 27 $\mu m^2$ on XY plane. The process parameters were progressively optimized for each formulation, according to its characteristics and its reactivity, and they are reported in Table 3. Final printing parameters were determined when acceptable CAD fidelity was achieved. After the 3D Printing process was completed, the objects were removed from the building platform and immersed in ethanol for washing. The samples underwent a post-curing process for 5 min in a UV curing device (light intensity 12 $mW{\cdot}cm^{-2}$).

## Characterization

**Photorherology**. *An* Anton Paar MCR 302 parallel-plate rotational rheometer has been used, equipped with a lamp emitting in the UV range (Hamamtsu Lc8, light intensity 20 $mW{\cdot}cm^{-2}$). The formulations were tested with a gap of 0.2 mm. Oscillation tests were carried out at room temperature with a constant frequency of 1 Hz and an amplitude of 1%, deriving from the preliminary test in which the linear viscoelastic region was determined. The lamp was switched on 60 s after the beginning of each test.

*Attenuated total reflectance Fourier transform infrared spectroscopy* (*ATR-FT-IR*) was used to evaluate the degree of conversion of the double bonds of the monomers. The experiments were conducted on a drop of formulation and on its respective printed sample using a Thermo Scientific Nicolet iS50 FTIR Spectrometer (Milano, Italy) equipped with a diamond crystal ATR accessory. For each sample, 64 spectra were collected in the range of 2000–400 $cm^{-1}$, with a resolution of 4 $cm^{-1}$. Different peaks were analyzed for determining the conversion: 1720 $cm^{-1}$ stretching of carbonyl in PEGDA (normalizing peak for calculation of acrylate conversion), 1640 $cm^{-1}$ stretching of carbon double bonds in the acrylic groups, 1350 $cm^{-1}$ *cis-trans* transition in (trifluoromethanesulphonyl)imide group (normalizing peak for calculation of vinyl conversion), 915 $cm^{-1}$ rocking of $CH_2$ vibration in vinyl group. The conversion was calculated by comparing the area of the peak of interest before and after the polymerization, divided by the area of the corresponding reference peak.

**Insoluble fraction evaluation (gel content)**. The insoluble fraction of the cured products was determined as described elsewhere[78]. Briefly, the samples were held in a metallic net, weighed, and immersed in chloroform for 24 h at RT to dissolve the not crosslinked polymer (soluble fraction). After, the samples were removed from the immersion bath and dried in a vacuum oven (80 °C, 100 mbar) until no mass variation was detected; the final weight was then evaluated. The gel content (GC%) was determined as reported in Eq. 1, and the results were averaged over three measurements.

$$GC\% = \left(\frac{\text{Final weight}}{\text{initial weight}}\right) \cdot 100 \quad (1)$$

*Dynamic Mechanical Thermal Analysis (DMTA)* was carried out using a Tritec 2000 DMA (Triton Technology). All the analyses have been performed at constant frequency (1 Hz) and with a temperature ramp of 3 °C per minute, starting from −40 °C to 100 °C The evolution of both the conservative and loss moduli (E' and E", respectively) and the damping factor (tan δ) during the temperature ramp was recorded. The glass transition temperature ($T_g$) was taken as the temperature corresponding to the maximum of tan δ peak.

**Optical Microscope and Field Emission Scanning Electron Microscope (FESEM)**. In order to evaluate the quality of the 3D printed objects, especially the ones characterized by more complex shapes, these were observed in detail thanks to optical microscope (Leica DFC340 FX) and FESEM imaging performed with a Zeiss Supra 40 on samples coated with a thin film of platinum.

**3D scanning**. The CAD fidelity was evaluated by employing E3 scanner (3Shape). Printed objects were first covered with talcum powder to properly diffract light. Afterward, the physical objects were digitalized, obtaining *.stl files. The so-obtained digital files were then compared with the original digital model using the equipment software. The results of the comparative analyses were displayed as a heatmap, showing the geometrical deviation from the reference model.

*Gravimetric adsorption measurements* were performed by evaluating the materials' Absorption Capacity as reported in Eq. 2, where m is the sample's mass measured before and after VOC exposure. The analyses were performed in two different set-ups.

$$Absorption\ Capacity = \left(\frac{m_f - m_i}{m_i}\right) \cdot 100 \quad (2)$$

The first one is designed for preliminary evaluations of the materials' behavior in an atmosphere saturated with the evaluated VOC. The set-up consists of sealed jars in which a 3D-printed sample and a smaller open jar containing the liquid VOC are positioned. The closed containers were then put in an oven at 40 °C for 24 h to enhance VOC evaporation. This test was performed in triplicate.

According to the second set-up, absorption of acetone (Ac) and acetonitrile (Acn) was evaluated using the outgassing station of an ASAP 2020 instrument (Micromeritics), which consists of two cells, one containing the sample and the other the solvent. These cells are connected to each other, to a vacuum system, and to two pressure sensors. A schematic representation of the station is provided in the Supporting Information (Fig. S10). Before exposure to pure solvent vapors (at an equilibrium pressure of 174 mbar for Ac and 90 mbar for Acn), the samples were degassed under vacuum for 2 h (residual pressure < $1.0 \times 10^{-2}$ mbar). A weight loss of less than 1.0% was observed for all samples after the pre-treatment. The mass of the outgassed 3D-printed samples (kept under vacuum) was subtracted from the mass after vapor adsorption to determine the Ac and Acn gravimetric adsorption capacity. As a tare, the weight of an empty cell filled to the same pressure as Ac or Acn was used. Before vapor dosing, the liquid solvents were de-aerated using on-line freeze-pump-thaw cycles performed at liquid nitrogen temperature.

*FT-IR measurements* were performed in transmission mode using a Bruker Tensor 27 spectrometer equipped with a liquid nitrogen-cooled mercury–cadmium–telluride (MCT) detector, operating at 2 $cm^{-1}$ resolution. Vacuum pre-treatment and solvent dosage were carried out using a standard glass vacuum frame in an IR cell equipped with KBr windows. IR transparent Silicon Wafers (Siltronix, Boron doped P-type, 20–30 Ω·cm) were coated with a thin polymer film using a wire wound bar and were irradiated in a Nitrogen atmosphere with UV-light (Hamamatsu LC8 lamps). The Si-supported films were outgassed for 1 h under secondary vacuum (residual $P < 0.1$ Pa) at RT before adsorption/desorption experiments. Before vapor dosing, the liquid solvents were de-aerated using on-line freeze-pump-thaw cycles performed at liquid nitrogen temperature. IR spectra were recorded after dosing increasing amounts (5 min equilibration time) of Ac (≥99%, Merck, ca. 4–175 mbar maximum equilibrium pressure) or Acn (>99.5%, Merck, ca. 1–90 mbar maximum equilibrium pressure) onto the outgassed samples. Subsequently, the samples were outgassed under vacuum at beam temperature (ca. 20 min in situ). Blank experiments

were also performed on a clean silicon wafer and with an empty cell filled with different vapor pressures.

To obtain a semi-quantitative comparison of the adsorbed amount, spectra of PEGDA-containing samples were normalized with respect to the integrated absorbance of $\nu_{CO}$ band, considering that the number of C=O groups per unit mass in PEGDA250 is ca. 2.3 times than that of PEGDA575. Spectra of $Bil_{10}$-$Mil_{90}$ samples were normalized to those of $P_5$-$Mil_{90}$ with respect to the integrated absorbance of the envelope band in the 3200–3000 $cm^{-1}$ range due to imidazolium ring modes (considering that the number of rings per unit mass in B.IL is double that in M.IL).

The spectra of adsorbed species are reported as subtraction spectra, i.e., obtained by subtracting the IR spectrum of the naked sample (before vapor adsorption).

## Data availability

All data needed to evaluate the conclusions in the paper are present in the paper and/or the Supplementary Materials. Additional data related to this paper may be requested from the corresponding author.

Received: 20 February 2025; Accepted: 31 May 2025;
Published online: 26 July 2025

## References

1. Baskaran, D., Dhamodharan, D., Behera, U. S. & Byun, H. S. A comprehensive review and perspective research in technology integration for the treatment of gaseous volatile organic compounds. *Environ. Res.* **251**, 118472 (2024).
2. Li, A. J., Pal, V. K. & Kannan, K. A review of environmental occurrence, toxicity, biotransformation and biomonitoring of volatile organic compounds. *Environ. Chem. Ecotoxicol.* **3**, 91–116, (2021).
3. Ghobakhloo, S., Khoshakhlagh, A. H., Morais, S. & Mazaheri Tehrani, A. Exposure to Volatile Organic Compounds in Paint Production Plants: Levels and Potential Human Health Risks. *Toxics* **11**, 111 (2023).
4. Singh, B. P. et al. Substantial Changes in Selected Volatile Organic Compounds (VOCs) and Associations with Health Risk Assessments in Industrial Areas during the COVID-19 Pandemic. *Toxics* **11**, 165 (2023).
5. Wahlang, B. et al. Associations between residential volatile organic compound exposures and liver injury markers: The role of biological sex and race. *Environ. Res.* **221**, 115228 (2023).
6. Li, Y. et al. Comparison of the ozone formation mechanisms and VOCs apportionment in different ozone pollution episodes in urban Beijing in 2019 and 2020: Insights for ozone pollution control strategies. *Sci.Total Environ.* **908**, 168332 (2024).
7. Settimo, G., Yu, Y., Gola, M., Buffoli, M. & Capolongo, S. Challenges in IAQ for Indoor Spaces: A Comparison of the Reference Guideline Values of Indoor Air Pollutants from the Governments and International Institutions. *Atmosphere (Basel)* **14**, 633 (2023).
8. Settimo, G., Manigrasso, M. & Avino, P. Indoor air quality: A focus on the european legislation and state-of-the-art research in Italy. *Atmosphere (Basel)* **11**, 370 (2020).
9. Li, S., Lin, Y., Liu, G. & Shi, C. Research status of volatile organic compound (VOC) removal technology and prospect of new strategies: a review. *Environ. Sci.: Process. Impacts* **25**, 727–740, (2023).
10. Zhu, L., Shen, D. & Luo, K. H. A critical review on VOCs adsorption by different porous materials: Species, mechanisms and modification methods. *J. Hazard. Mater.* **389**, 122102 (2020).
11. Siu, B., Chowdhury, A. R., Yan, Z., Humphrey, S. M. & Hutter, T. Selective adsorption of volatile organic compounds in metal-organic frameworks (MOFs). *Coord. Chem. Rev.* **485**, 215119 (2023).
12. Zhang, W. et al. Adsorption and desorption mechanism of aromatic VOCs onto porous carbon adsorbents for emission control and resource recovery: Recent progress and challenges. *Environ. Sci.: Nano* **9**, 81–104, https://doi.org/10.1039/d1en00929j (2022).
13. Salar-García, M. J., Ortiz-Martínez, V. M., Hernández-Fernández, F. J., de los Ríos, A. P. & Quesada-Medina, J. Ionic liquid technology to recover volatile organic compounds (VOCs). *J. Hazard. Mater.* **321**, 484–499, (2017).
14. Moufawad, T., Costa Gomes, M. & Fourmentin, S. Deep eutectic solvents as absorbents for VOC and VOC mixtures in static and dynamic processes. *chem. Eng. J.* **448**, 137619 (2022).
15. Guo, Y., Wen, M., Li, G. & An, T. Recent advances in VOC elimination by catalytic oxidation technology onto various nanoparticles catalysts: a critical review. *Appl. Catal B* **281**, 119447 (2021).
16. Gao, W. et al. Mesoporous molecular sieve-based materials for catalytic oxidation of VOC: A review. *J. Environ. Sci.***125**, 112–134, (2023).
17. Chaudhary, D. K., Park, J. H., Kim, P. G., Ok, Y. S. & Hong, Y. Enrichment cultivation of VOC-degrading bacteria using diffusion bioreactor and development of bacterial-immobilized biochar for VOC bioremediation. *Environ Pollut* **320**, 121089 (2023).
18. Meena, M., Sonigra, P. & Yadav, G. Biological-based methods for the removal of volatile organic compounds (VOCs) and heavy metals. https://doi.org/10.1007/s11356-020-11112-4/Published.
19. Zhang, S. et al. Effect of calcium hydroxide on the characteristics of volatile organic compounds emission during sewage sludge incineration. *Environ. Prog. Sustain Energy* **42**, e14016 (2023).
20. Mu, Y. & Williams, P. T. Recent advances in the abatement of volatile organic compounds (VOCs) and chlorinated-VOCs by non-thermal plasma technology: A review. *Chemosphere* **308**, 136481 (2022).
21. Zhang, W., Li, G., Chen, Z., Shang, Z. & Xu, P. Efficient capture of benzene and its homologues volatile organic compounds with protic [MIM][NTF2] and aprotic [EMIM][NTF2] ionic liquids: Experimental and computational thermodynamics. *J. Environ. Chem. Eng.* **11**, 111124 (2023).
22. Shang, Z. et al. Ionic-liquid-assisted capture of volatile low-carbon alcohols in printing plant exhaust gas. *ACS Sustain Chem. Eng.* **12**, 5661–5674 (2024).
23. Sun, Y. et al. A novel Copper(I)-based supported ionic liquid membrane with high permeability for ethylene/ethane separation. *Ind. Eng. Chem. Res.* **56**, 741–749 (2017).
24. Alaei Shahmirzadi, M. A., Kargari, A. & Matsuura, T. "Tai Chi" philosophy driven dual-network ionogel membrane comprised of ionic guests in a multifunctional host for propylene/propane separation. *J. Mol. Liq.* **384**, 122216 (2023).
25. Sanchez, C. M., Song, T., Brennecke, J. F. & Freeman, B. D. Hydrogen stable supported ionic liquid membranes with silver carriers: propylene and propane permeability and solubility. *Ind. Eng. Chem. Res.* **59**, 5362–5370 (2020).
26. Dou, H. et al. Supported ionic liquid membranes with high carrier efficiency via strong hydrogen-bond basicity for the sustainable and effective olefin/paraffin separation. *Chem. Eng. Sci.* **193**, 27–37 (2019).
27. Gujjala, L. K. S. et al. Advances in ionic liquids: Synthesis, environmental remediation and reusability. *J. Mol. Liq.* **396**, 123896 (2024).
28. Elmobarak, W. F. et al. Current status of $CO_2$ capture with ionic liquids: Development and progress. *Fuel* **344**, 128102 (2023).
29. Yan, X., Anguille, S., Bendahan, M. & Moulin, P. Ionic liquids combined with membrane separation processes: A review. *Sep. Purif. Technol.* **222**, 230–253 (2019).
30. Goudarzi, F. & Rahimpour, M. R. Hybrid membranes, liquid/solid, for the enhancement of membrane gas selectivity. The example of ionic liquid membrane. *Current Trends and Future Developments on (Bio-) Membranes: Modern Approaches in Membrane Technology for Gas Separation and Water Treatment* 331–347 (2024) https://doi.org/10.1016/B978-0-323-99311-1.00018-0.
31. Lebedeva, O., Kultin, D. & Kustov, L. Advanced research and prospects on polymer ionic liquids: trends, potential and application. *Green Chem.* **25**, 9001–9019 (2023).

32. Doblinger, S., Hay, C. E., Tomé, L. C., Mecerreyes, D. & Silvester, D. S. Ionic liquid/poly(ionic liquid) membranes as non-flowing, conductive materials for electrochemical gas sensing. *Anal. Chim. Acta* **1195**, 339414 (2022).
33. Roppolo, I. et al. Digital light processing 3D printing of polymerizable ionic liquids towards carbon capture applications. *React. Funct. Polym.* **202**, 105962 (2024).
34. Zhang, Y. et al. Highly sensitive gas-sensing films for volatile organic acids from Imidazolium-Based Poly(ionic liquid)s. *J. Nanosci. Nanotechnol.* **20**, 3588–3597 (2019).
35. Karunaweera, C., Li, P., Gin, D. L. & Noble, R. D. Stable, long-term, high-temperature, and high-pressure operation of poly(ionic liquid)-ionic liquid membranes made with ionic-liquid-based multifunctional cross-linkers for $CO_2/CH_4$ separation. *Ind. Eng. Chem. Res* **61**, 12180–12189 (2022).
36. Bara, J. E. et al. Synthesis and performance of polymerizable room-temperature ionic liquids as gas separation membranes. *Ind. Eng. Chem. Res* **46**, 5397–5404 (2007).
37. Durga, G. et al. Ionic liquids: From a solvent for polymeric reactions to the monomers for poly(ionic liquids). *J. Mol. Liq.* **335**, 116540 (2021).
38. Zhang, F. et al. The recent development of vat photopolymerization: A review. *Addit. Manuf.* **48**, 102423 (2021).
39. Miralles-Comins, S., Zanatta, M. & Sans, V. Advanced formulations based on poly(ionic liquid) materials for additive manufacturing. *Polymers* **14**, 5121 (2022).
40. Nulwala, H., Mirjafari, A. & Zhou, X. Ionic liquids and poly(ionic liquid)s for 3D printing – A focused mini-review. *Eur. Polym. J.* **108**, 390–398, (2018).
41. Hosseinabadi, H. G. et al. Ink material selection and optical design considerations in DLP 3D printing. *Appl. Mater. Today* **30**, 101721 (2023).
42. Palmara, G., Frascella, F., Roppolo, I., Chiappone, A. & Chiadò, A. Functional 3D printing: Approaches and bioapplications. *Biosensors Bioelectron.* **175**, 112849 (2021).
43. Salas, A., Zanatta, M., Sans, V. & Roppolo, I. Chemistry in light-induced 3D printing. *ChemTexts* **9**, 1–16 (2023).
44. Roppolo, I., Caprioli, M., Pirri, C. F. & Magdassi, S. 3D Printing of Self-Healing Materials. *Adv. Mater.* **36**, 2305537 (2024).
45. Park, S., Shou, W., Makatura, L., Matusik, W. & Fu, K. 3D printing of polymer composites: Materials, processes, and applications. *Matter* **5**, 43–76 (2022).
46. Dixit, C. K., Kadimisetty, K. & Rusling, J. 3D-printed miniaturized fluidic tools in chemistry and biology. *TrAC - Trends Anal. Chem.* **106**, 37–52, (2018).
47. Mo, X., Ouyang, L., Xiong, Z. & Zhang, T. Advances in digital light processing of hydrogels. *Biomed. Mater.* **17**, 042002 (2022).
48. Li, H. et al. Digital light processing (DLP)-based (bio)printing strategies for tissue modeling and regeneration. *Aggregate* **4**, e270 (2023).
49. Zhang, X. et al. High tensile properties, wide temperature tolerance, and DLP-printable eutectogels for microarrays wearable strain sensors. *Chem. Eng. J.* **481**, 149004 (2024).
50. Mogli, G. et al. Self-powered integrated tactile sensing system based on ultrastretchable, self-healing and 3D printable ionic conductive hydrogel. *Adv. Funct. Mater.* **34**, 2307133 (2024).
51. Yi, J., Yang, S., Yue, L. & Lei, I. M. Digital light processing 3D printing of flexible devices: actuators, sensors and energy devices. *Microsyst. Nanoeng.* **11**, 51 (2025).
52. Chekkaramkodi, D., Jacob, L., Shebeeb, C. M., Umer, R. & Butt, H. Review of vat photopolymerization 3D printing of photonic devices. *Addit. Manuf.* **86**, 104189 (2024).
53. Cosola, A. et al. 4D printing of multifunctional devices induced by synergistic role of magnetite and silver nanoparticles in polymeric nanocomposites. *Adv. Funct. Mater.* https://doi.org/10.1002/adfm.202406226 (2024).
54. Andreu, A. et al. 4D printing materials for vat photopolymerization. *Addit. Manuf.* **44**, 102024 (2021).
55. Maciel, V. G., Wales, D. J., Seferin, M. & Sans, V. Environmental performance of 3D-Printing polymerisable ionic liquids. *J. Clean. Prod.* **214**, 29–40 (2019).
56. Wales, D. J. et al. 3D-printable photochromic molecular materials for reversible information storage. *Adv. Mater.* **30**, 1800159 (2018).
57. Miralles-Comins, S. et al. Development of high-resolution 3D printable polymerizable ionic liquids for antimicrobial applications. *Device* **2**, 100224 (2024).
58. Narupai, B. et al. 3D printing of ionic liquid polymer networks for stretchable conductive sensors. *Adv. Mater. Technol.* **8**, 2300226 (2023).
59. Lee, T. Y. et al. The kinetics of vinyl acrylate photopolymerization. *Polymer***44**, 2859–2865 (2003).
60. Guizard, C. et al. VOC vapour transport properties of new membranes based on cross-linked fluorinated elastomers. *Sep. Purif. Technol.* **22-23**, 23–30 (2001).
61. Zhao, X. et al. High-performance silicone membranes for VOC/$N_2$ separation: a new crosslinking strategy via octyl-grafted Poly(hydromethylsiloxane). *Ind. Eng. Chem. Res.* **62**, 13974–13987 (2023).
62. Li, X. et al. Adsorption materials for volatile organic compounds (VOCs) and the key factors for VOCs adsorption process: A review. *Sep. Purif. Technol.* **235**, 116213 (2020).
63. Lee, D. G., Kim, J. H. & Lee, C. H. Adsorption and thermal regeneration of acetone and toluene vapors in dealuminated Y-zeolite bed. *Sep Purif. Technol.* **77**, 312–324 (2011).
64. Zhou, X. et al. A novel MOF/graphene oxide composite GrO@MIL-101 with high adsorption capacity for acetone. *J. Mater. Chem. A Mater.* **2**, 4722–4730 (2014).
65. Cheng, C. et al. Sago cycas–based hierarchical–structured porous carbon for adsorption of acetone vapour: preparation, characterization and performance. *Environ. Sci. Pollut. Res.* **29**, 19165–19175 (2022).
66. Roth, C. et al. Hydrogen bonding in ionic liquids probed by linear and nonlinear vibrational spectroscopy. *N. J. Phys.* **14**, 105026 (2012).
67. Crocellà, V., Cerrato, G., Magnacca, G. & Morterra, C. Adsorption of acetone on nonporous and mesoporous silica. *J. Phys. Chem. C.* **113**, 16517–16529 (2009).
68. Zaki, M. I., Hasan, M. A., Al-Sagheer, F. A. & Pasupulety, L. Surface chemistry of acetone on metal oxides: IR observation of acetone adsorption and consequent surface reactions on silica−alumina versus silica and alumina. *Langmuir* **16**, 430–436 (1999).
69. Kubelková, L., Čejka, J. & Nováková, J. Surface reactivity of ZSM-5 zeolites in interaction with ketones at ambient temperature (a FT-IR. study). *Zeolites* **11**, 48–53 (1991).
70. Colthup, N. B., Daly, L. H. & Wiberley, S. E. *Introduction to Infrared and Raman Spectroscopy*. (Academic Press, 1975).
71. Cimatu, K. L. A. et al. Polymer-solvent interaction and conformational changes at a molecular level: Implication to solvent-assisted deformation and aggregation at the polymer surface. *J. Colloid Interface Sci.* **616**, 221–233 (2022).
72. Venkateswarlu, P. The rotation-vibration spectrum of methyl cyanide in the region 1.6 μ—20 μ. *J. Chem. Phys.* **19**, 293–298 (1951).
73. Salla, I., Montanari, T., Salagre, P., Cesteros, Y. & Busca, G. Fourier transform infrared spectroscopic study of the adsorption of CO and Nitriles on Na−Mordenite: Evidence of a new interaction. *J. Phys. Chem. B* **109**, 915–922 (2004).
74. Trombetta, M. et al. Solid acid catalysts from clays: Evaluation of surface acidity of mono- and bi-pillared smectites by FT-IR spectroscopy measurements, NH3-TPD and catalytic tests. *Appl Catal. A Gen.* **193**, 55–69 (2000).
75. Busca, G., Montanari, T., Bevilacqua, M. & Finocchio, E. Removal and recovery of nitriles from gaseous streams: An IR study of acetonitrile adsorption on and desorption from inorganic solids. *Colloids Surf. A Physicochem. Eng. Asp.* **320**, 205–212 (2008).
76. Thommes, M. et al. Physisorption of gases, with special reference to the evaluation of surface area and pore size distribution (IUPAC Technical Report). *Pure Appl. Chem.* **87**, 1051–1069 (2015).

77. Gussoni, M., Rui, M. & Zerbi, G. Electronic and relaxation contribution to linear molecular polarizability. An analysis of the experimental values. *J. Mol. Struct.* **447**, 163–215 (1998).
78. Gastaldi, M. et al. Thermochromic photoluminescent 3D printed polymeric devices based on copper-iodide clusters. *Addit. Manuf.* **49**, 102504 (2022).

## Acknowledgements

A.C. acknowledges the funding support from the European Union – Next Generation EU, component M4C2, investimento 1.1. PRIN 2022 PNRR Project "3D VOCe" code P2022JWF3P and Fondazione di Sardegna, FdS2022 Project "3D printed optical VOC sensors for indoor air quality evaluation".

## Author contributions

Conceptualization: I. Roppolo and A. Chiappone. Methodology: M. Aramandi. Experiment: B. Tosetto, A. Chiappone. Data analysis: I. Roppolo, M. Armandi Writing—original draft: M. Armandi, B. Tosetto—review & editing: I. Roppolo, A. Chiappone.

## Competing interests

The authors declare no competing interests.

## Additional information

**Supplementary information** The online version contains supplementary material available at https://doi.org/10.1038/s44334-025-00041-0.

**Correspondence** and requests for materials should be addressed to Ignazio Roppolo.

**Reprints and permissions information** is available at http://www.nature.com/reprints

**Publisher's note** Springer Nature remains neutral with regard to jurisdictional claims in published maps and institutional affiliations.

**Open Access** This article is licensed under a Creative Commons Attribution-NonCommercial-NoDerivatives 4.0 International License, which permits any non-commercial use, sharing, distribution and reproduction in any medium or format, as long as you give appropriate credit to the original author(s) and the source, provide a link to the Creative Commons licence, and indicate if you modified the licensed material. You do not have permission under this licence to share adapted material derived from this article or parts of it. The images or other third party material in this article are included in the article's Creative Commons licence, unless indicated otherwise in a credit line to the material. If material is not included in the article's Creative Commons licence and your intended use is not permitted by statutory regulation or exceeds the permitted use, you will need to obtain permission directly from the copyright holder. To view a copy of this licence, visit http://creativecommons.org/licenses/by-nc-nd/4.0/.

© The Author(s) 2025